Dissolution heterogeneity observed in anisotropic ruthenium dioxide nanocrystals via liquid-phase transmission electron microscopy

Keywords: RuO_2, LP-TEM, heterogeneity, dissolution

Authors: S. Avery Vigil[1], Ivan A. Moreno-Hernandez[1]

Affiliations:

[1]Department of Chemistry, Duke University, Durham, North Carolina 27708, United States

Abstract

Noble metal oxides such as ruthenium dioxide are highly active electrocatalysts for anodic reactions in acidic electrolytes, but dissolution during electrochemical operation impedes wide-scale application in renewable energy technologies. Improving the fundamental understanding of the dissolution dynamics of application-relevant morphologies such as nanocrystals is critical for grid-scale implementation of these materials. Herein we report the nanoscale heterogeneity observed via liquid phase transmission electron microscopy during ruthenium dioxide nanocrystal dissolution under oxidizing conditions. Single-crystalline ruthenium dioxide nanocrystals enabled direct observation of dissolution along different crystallographic facets, allowing an unprecedented direct comparison of crystal facet stability. The nanoscale observations revealed substantial heterogeneity in the relative stability of crystallographic facets across different nanocrystals, attributed to nanoscale strains present in these crystals. These findings highlight the importance of nanoscale heterogeneity in determining macroscale properties such as electrocatalyst stability and provide a characterization methodology that can be integrated into next-generation electrocatalyst discovery efforts.

Introduction

The electrochemical production of chemical feedstocks is a promising approach to decarbonize the energy and chemical sectors. Valuable chemical feedstocks such as hydrocarbons, ammonia, and hydrogen can be generated via reduction of carbon dioxide, nitrogen, and water, respectively.[1-9] These cathodic reactions are necessarily coupled to an anodic reaction such as the oxygen evolution reaction (OER). The sluggish kinetics of the OER result in substantial energy losses during the operation of electrolyzers, limiting the overall efficiency of the complete fuel-forming reactions described above.[7-13] In acidic electrolytes, the use of noble metal oxide electrocatalysts is required due to their moderately high stability and activity. However, electrocatalysts for the OER often undergo structural changes that can lead to loss of activity, mandating high catalyst loadings of scarce elements.[14-16] Much of our understanding of these vital structural phenomena comes from macroscopic techniques and post-mortem analyses of electrocatalysts, which conceal the connection between nanoscale dynamics and macroscopic properties and limit the ability to control electrocatalytic behavior.[9,17-19] A better understanding of the dissolution dynamics of electrocatalytic materials is necessary to inform the design of next generation electrocatalysts for the OER or related anodic reactions such as the chlorine evolution reaction (CER).

Ruthenium(IV) oxide (RuO_2) is a highly active electrocatalyst for the OER and CER but spontaneously undergoes dissolution to ruthenium tetroxide (RuO_4) at electrochemical potentials above 1.387 V vs. NHE.[20-22] Studies on bulk oriented RuO_2 films reveal facet-dependent dissolution rates attributed to the anisotropic structure of rutile-type RuO_2, which has different surface coordination depending on which crystal orientation is exposed to the electrolyte.[19,22-25] While the ensemble techniques used to elucidate these dissolution rates provide essential macroscopic dissolution information, nanoscale techniques are needed to analyze these materials in technologically relevant morphologies such as nanoparticles. Electrocatalytic nanoparticles can exhibit dramatically different properties compared to their bulk counterparts, in part due to the substantial increase of surface effects in nanomaterials.[26]

Liquid phase transmission electron microscopy (LP-TEM) performed with graphene liquid cells enables direct observation of nanoscale structural dynamics with near-atomic spatial resolution and high temporal resolution.[27-29] Recent advances in our understanding of the electron-beam induced chemical reactivity generated during LP-TEM imaging have made it possible to modulate the reactive environment via redox additives to a high degree of electrochemical precision.[29] Additionally, *in-situ* observations of redox chemistry have substantially improved our ability to accurately model the complex chemical

environment created during LP-TEM.[27,28] These advances allow for the investigation of systems comprised of multiple elements, such as RuO_2, utilizing redox additives capable of generating electrochemical environments that lead to nanoscale structural dynamics.[29]

Herein we report the spatiotemporal dissolution dynamics of several anisotropic RuO_2 nanocrystals at the individual nanocrystal level with LP-TEM. Using Fe(III) as a redox additive, radical species generated by electron-beam induced water radiolysis are scavenged to generate a redox couple that is capable of driving the RuO_2/RuO_4 dissolution reaction. Single-crystalline nanocrystals of rutile RuO_2 with well-defined facets are used to test orientation-dependent dissolution dynamics, allowing for simultaneous observation of different crystallographic facets during dissolution of single RuO_2 nanocrystals for the first time. Our study indicates that the *ensemble* dissolution rates of RuO_2 nanocrystal facets increase from (110), (111), to (001). However, the relative stability observed at the individual nanocrystal level exhibits substantial heterogeneity. Geometric phase analysis measurements on single-crystalline RuO_2 nanocrystals reveal substantial heterogeneity in the location and intensity of strain within individual nanocrystals. Together, these results suggest the presence of structural heterogeneities that influence stability under operation. The experimental results and analytical methods reported herein further the understanding of nanoscale heterogeneity on material stability through direct observation of nanoscale dissolution dynamics of oxides for anodic reactions.

Experimental

Ruthenium dioxide nanocrystal synthesis

Ruthenium dioxide (RuO_2) nanocrystals were synthesized according to a previously reported chemical vapor deposition method with minor modifications.[30] A 6 mL quartz boat was loaded with 27.9 mg of commercial RuO_2 powder (Millipore Sigma, 99.9%) into the center of a tube furnace with a 22 mm inner diameter quartz tube. Substrates were loaded onto a 6 mL quartz boat placed just outside of the insulated region of the tube furnace. Ultra-high purity Ar and O_2 were flowed at 300 sccm and 1600 sccm, respectively, and the furnace was raised to 1050°C at 50°C/min. The temperature was held for 4 hours and subsequently cooled to room temperature. Copper(II) oxide powder (CuO, Thermo Scientific, 99.0%) and prepared antimony-doped tin oxide thin-films on quartz (ATO) were utilized as substrates for the synthesis of unsupported RuO_2 nanocrystals and supported RuO_2 nanocrystals, respectively. Unsupported and supported RuO_2 nanocrystals were grown separately. Approximately 100 mg of CuO was used for each synthesis of unsupported RuO2 nanocrystals, and ~ 6 pieces of 0.780 cm^2 ATO were used for each synthesis of supported RuO_2 nanocrystals. After being allowed to cool to room temperature, the RuO_2 nanocrystals on CuO were transferred to a 15 mL centrifuge tube. The CuO support was selectively etched by adding 6 mL of 2 M HCl. The solution was sonicated and washed several times with water via centrifugation to remove any dissolved copper. The resultant nanocrystals were dispersed in water and used without further purification. The RuO_2 nanocrystals grown on ATO were utilized directly as electrodes to ascertain electrochemical activity. The RuO_2 loading was estimated to be 0.559 mg cm^{-2} based on the weight of the ATO samples before and after RuO_2 nanocrystal deposition.

Graphene-coated transmission electron microscopy grid preparation

Graphene-coated TEM grids were fabricated via previously reported methods with slight modifications.[31] Copper foil with 3-5 layers of graphene (ACS Material) was washed once by placing it an acetone bath prepared in a glass petri dish at 50 ºC for 5 minutes to remove surface impurities. After one hour of drying, the graphene-coated copper foil was flattened by compressing it between two glass slides and a folded wipe. The wipe was sequentially unfolded to further flatten the copper foil as described in previous work.[31] Gold TEM grids (100x400 Mesh 1.3 Quantifoil, Holey Carbon, Structure Probe, Inc.) were placed Quantifoil side down on the graphene. One out of three gold TEM grids were sliced in half with a clean razor blade prior to being placed down on the graphene. A few µL of isopropanol was used to

ensure proper adherence of the Quantifoil to the graphene-coated copper foil, and the grids were arranged on the substrate by carefully moving them with a pipette tip. The isopropanol was allowed to dry for two hours, and the copper foil was subsequently floated on top of a bath of sodium persulfate (100 mg per mL) prepared in a glass petri dish, and the copper foil was allowed to etch overnight. The grids were subsequently removed with a glass slide, transferred to a petri dish with DI water, retrieved with tweezers, and allowed to dry fully prior to utilization.

Electron microscopy characterization

Electron microscopy characterization was primarily carried out on an FEI Tecnai G^2 Twin equipped with a GATAN OneView operating at 200 keV with a $LaBr_6$ filament located at the Shared Materials Instrumentation Facility at Duke University. Characterization requiring aberration correction or STEM imaging (such as elemental mapping) was performed using a ThermoFisher Titan 80-300 operated at 200 kV using an FEI double tilt holder with a molybdenum retention clip, located at the Analytical Instrumentation Facility at North Carolina State University.

Liquid phase electron microscopy data acquisition

Liquid phase videos were collected on the FEI Tecnai G^2 Twin transmission electron microscope equipped with a Gatan OneView *in situ* camera operating at an accelerating voltage of 200 kV and a spot size of 1. Video frames were collected at a binned resolution of 2048x2048 pixels, a magnification of 100kx, and an exposure time of 0.01 s. The pixel resolution was 0.2125 nm per pixel. Every tenth frame was kept, resulting in a frame being collected every 0.1 s (10 frames per second). The electron dose rate of the microscope was adjusted with a custom Digital Micrograph script that determined the relationship between condenser lens value and electron dose rate as descripted in a previous publication.[32] The electron beam was fully spread at a magnification between 20-100kx to search for adequate samples within the graphene liquid cell. Once a sample was found, the imaging area was moved approximately 1,000 nm away from the region of interest, the electron dose rate was set to 2000 $e^-/A^2 \cdot s$, and the microscope was focused using the OneView camera. This step of the data acquisition process is important to minimize the need to adjust the focus during video collection. Subsequently, the electron beam was spread to lower the electron dose rate and the stage was moved back to the region of interest. The lookback feature of the OneView camera was used to continuously collect the previous 30 seconds of data prior to video collection. The electron dose was set to 2000 e^- $Å^{-2}$ s^{-1} and videos of nanocrystal dissolution were collected for approximately 1 to 6 minutes.

Results & discussion

Characterization of ruthenium oxide nanocrystals

We observed the dissolution dynamics of rutile-type RuO_2 nanocrystals at the individual nanocrystal level via LP-TEM. Graphene liquid cells loaded with aqueous solutions containing Fe(III) and RuO_2 nanocrystals were utilized (Fig. 1a). Single-crystalline and low-index faceted RuO_2 nanocrystals were synthesized to elucidate the effect of the anisotropic rutile-type structure on the dissolution dynamics of RuO_2 (see Supplementary Information for detailed synthesis). Fig. 1b shows the high-angle annular dark field (HAADF) images and energy-dispersive x-ray spectroscopy (EDS) maps for an individual nanocrystal. The nanocrystal exhibits an anisotropic structure, with preferential growth along the (001) direction, resulting in sides terminated by (110) facets and tips terminated by a combination of (111) and (001) facets. The EDS maps indicate that the nanocrystals were uniformly composed of Ru and O (Fig. 1b). HAADF-STEM imaging at high magnification indicates that the nanocrystals solely consist of the rutile-type structure (Fig. 1c).
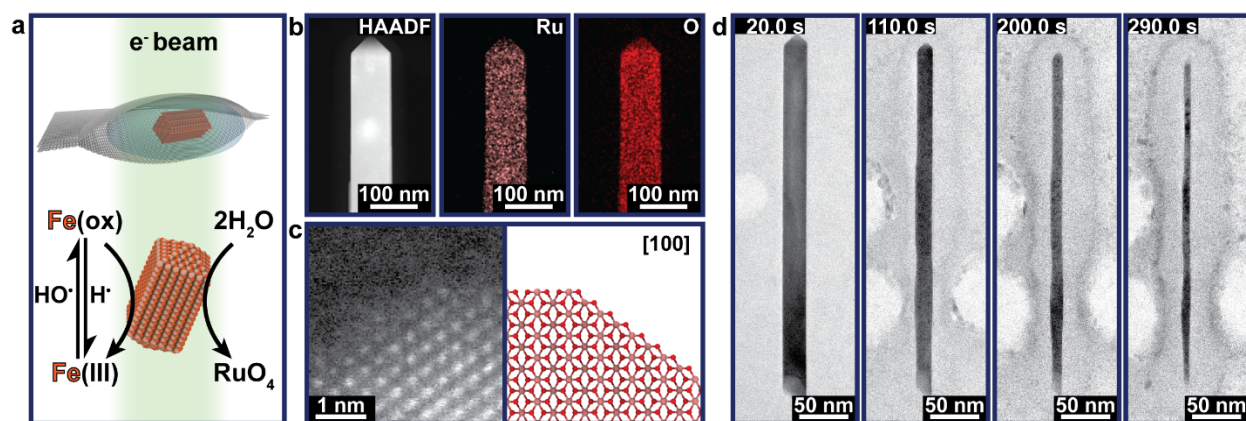
Fig. 1: Redox-mediated dissolution dynamics of RuO_2 nanocrystals. (a) Schematic of graphene liquid cell experiments: Fe(III) reacts with radiolysis products to generate high-valent Fe(ox), which creates an oxidative environment that converts RuO_2 to soluble products. (b) HAADF-STEM and EDS characterization of synthesized RuO_2 nanocrystals in the dry state. (c) High-magnification HAADF-STEM image of the RuO_2 nanocrystal tip and corresponding atomic model. (d) TEM image time series of a RuO_2 nanocrystal at an electron dose of 2,000 e⁻ Å⁻² s⁻¹ in a graphene liquid cell assembled with RuO_2 nanocrystals, 25 mM $FeCl_3$, 25 mM $MgCl_2$ and 100 mM HCl.

The RuO_2 nanocrystals were characterized with x-ray photoelectron spectroscopy (XPS), Raman spectroscopy, electrochemical techniques, scanning electron microscopy (SEM), high-resolution transmission electron microscopy (HRTEM), and selected-area electron diffraction (SAED) as detailed in the Supplementary Information. Fig. S1 shows XPS characterization of commercial RuO_2 and synthesized RuO_2 nanocrystals. The Ru 3d, C 1s, and O 1s signals were fit with established procedures for Ru-based compounds and were found to be adequately described by RuO_2 for both the commercial RuO_2 and synthesized RuO_2 nanocrystals (Table S1).[33] Fig. S2a verifies the presence of graphene on the TEM grids used in this study, as evidenced by a strong 2D peak at 2634 cm⁻¹.[34] Fig. S2b shows a Raman spectrum of synthesized RuO_2 nanocrystals suspended on a gold TEM grid from 400 to 800 cm⁻¹; the position of the E_g, A_{1g}, and B_{2g} bands of RuO_2 are consistent with a rutile structure and nanorod-like morphology.[35] Fig. S3 shows the electrochemical properties of RuO_2 grown on antimony-doped tin oxide (ATO) for water oxidation in 1.0 M perchloric acid and an SEM image of the nanocrystal morphology on ATO. The RuO_2 nanocrystals grown on ATO exhibited high activity towards water oxidation compared to the ATO substrate (Fig. S3a).

Radiolysis of iron-containing graphene liquid cells

Fig. 1d shows the dissolution of an individual RuO_2 nanocrystal using Fe(III) as a redox additive at an electron dose rate of 2,000 e⁻ Å⁻² s⁻. Under these conditions, RuO_2 was found to be unstable, undergoing dissolution along all crystal facets within several minutes of irradiating with the electron-beam (Supplementary Movies S1-S2). The dissolution rate was substantially slower than previous studies using Fe(III) as a redox mediator to oxidize noble metals, consistent with bulk-scale observations of enhanced material stability of oxides compared to metals under oxidizing environments.[36] The electrolyte used for all LP-TEM experiments was 25 mM $FeCl_3$, 25 mM $MgCl_2$, and 100 mM HCl unless otherwise indicated. Fe(III) was selected as a redox additive due to the requirement of a high electrochemical potential for this study, as RuO_2 undergoes oxidation in acid above 1.387 V vs. NHE.[20] Fe has multiple valence states, ranging from (II) to (VI), with Fe(VI) to Fe(IV) being highly oxidative (Table S2).[20] Previous studies have indicated that Fe(III) undergoes oxidation to high-valent Fe, Fe(ox), under electron-beam irradiation in graphene liquid cells.[37,38] A homogenous chemical reaction network model was developed based on a

kinetic model constructed by Schneider, et al. (Table S3).[39] The models indicate that all species reach a steady-state concentration in a timescale relevant to the graphene liquid cell experiments (Fig. S4). While high-valent Fe is known to spontaneously reduce to Fe(III) in acidic solutions, the simulations indicate that oxidation by primary radicals could compete with the reduction process and generate a steady-state concentration of high-valent Fe in the 10 mM range (Fig. S4). The effect of initial Fe(III) and Cl concentration on the steady-state concentrations was explored via 10,201 radiolysis simulations (Fig. S5). The simulations indicate that both Fe(III) and Cl additives act as radical scavengers, with both leading to a substantial decrease in the concentration of hydroxyl radicals and atomic hydrogen. The addition of both Fe(III) and Cl leads to competitive scavenging of primary radicals to produce high-valent Fe and oxidized Cl species (Fig. S5). The simulations suggest that Fe(IV) is the primary oxidant in concentrated Fe electrolytes (Fig. S4, S5). While direct observation of the oxidation state of Fe in this system was challenging, the observation of RuO_2 nanocrystal dissolution is consistent with spontaneous oxidation to RuO_4 via a redox reaction with a high-valent Fe species (Table S4). Control experiments without Fe(III) exhibit dissolution, which suggests that hydroxyl radicals or oxidized Cl species can be involved in the dissolution of RuO_2 (Fig. S6, Supplementary Movie S3). Species that are capable of spontaneously dissolving RuO_2 include $HO^\bullet$, Fe(IV) to Fe(VI), $Cl^\bullet$, and $Cl_2^{\bullet-}$ (Table S4).
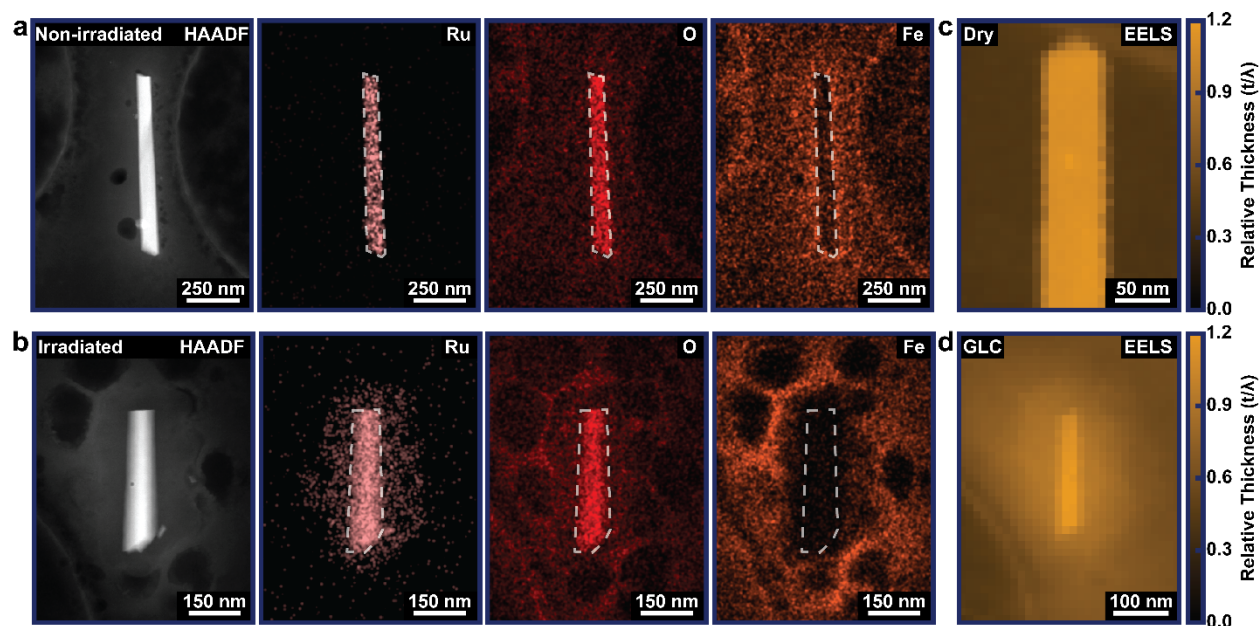

Fig. 2: EDS and EELS measurements of RuO_2 nanocrystals, dotted outlines indicate the perimeter of the RuO_2 nanocrystal as determined from the HAADF image. (a) EDS characterization of a RuO_2 nanocrystal in a graphene liquid cell without exposure to a high electron dose. (b) EDS characterization of a RuO_2 nanocrystal in a graphene liquid cell after irradiation at a high electron dose. (c) EELS relative thickness map of a dry RuO_2 nanocrystal suspended on a TEM grid. (d) EELS relative thickness map of the irradiated RuO_2 nanocrystal shown in (b).

Fig. 2 shows in-situ TEM-based spectroscopic characterization performed on graphene liquid cells before and after electron irradiation. Fig. 2a corresponds to the HAADF, Ru, O, and Fe maps collected for a RuO_2 nanocrystal in a graphene liquid cell prior to exposure to a high electron dose. Without irradiation, the Ru signal was localized to the high intensity region present in the HAADF image, which was consistent with the Ru only being present in the RuO_2 lattice of the nanocrystal. The O signal was intense in the nanocrystal region, consistent with the high concentration of O in the RuO_2 lattice, and evenly dispersed

through the pocket, consistent with H_2O being present around the RuO_2 nanocrystal. The Fe signal was similarly dispersed throughout the pocket, and notably diminished in the nanocrystal region. The EDS data indicated a homogenous initial condition for the liquid cell. Fig. 2b shows the corresponding HAADF image and EDS maps for a different RuO_2 nanocrystal in a graphene liquid cell after exposure to a high electron dose for several minutes. After irradiation there were significant differences in the distribution of elemental signals. The Ru signal was not localized within the nanocrystal and was instead also distributed in the electrolyte. The O signal remained well-dispersed after electron-beam irradiation. The Fe signal indicates that there was depletion of Fe in the vicinity of the RuO_2 nanocrystal. Fig. S7 shows the EDS data for the other electrolyte constituents, Mg and Cl. Mg was shown to have a similar dispersion to Fe, while Cl maintained a dispersion similar to that of O. The EELS log-log technique was utilized to obtain the relative thickness of both a RuO_2 nanocrystal suspended on a TEM grid and a RuO_2 nanocrystal in a graphene liquid cell (Fig. 2c-d).[40] The maximum relative thickness of the dry nanocrystal was found to be 1.1880 for a nanocrystal that was 50.2 nm wide, while the maximum relative thickness of the liquid cell was found to be 1.2024 for a nanocrystal that was 57.9 nm wide. The EELS maps indicate that there was a relatively thin liquid layer separating the facets facing the graphene sheets. The EELS data was utilized to verify the distribution of the electrolyte in the liquid cell (Fig. S8). Characteristic energy loss ranges were scanned to observe Fe and Cl distribution in the liquid cell; the signal from these ranges reflect the electrolyte distribution observed via EDS. Fig. S9 shows HRTEM and electron diffraction for RuO_2 nanocrystals that were either suspended on a dry TEM grid or inside of a graphene liquid cell. The RuO_2 nanocrystals were single crystalline in both the dry and graphene liquid cell environments, and near-atomic resolution could be obtained in both the dry and liquid state (Fig. S9). As shown in Fig. S9f, electron diffraction indicated the formation of Fe(III) chloride hexahydrate and Mg(II) chloride hexahydrate nanocrystals in the graphene liquid cell environment.
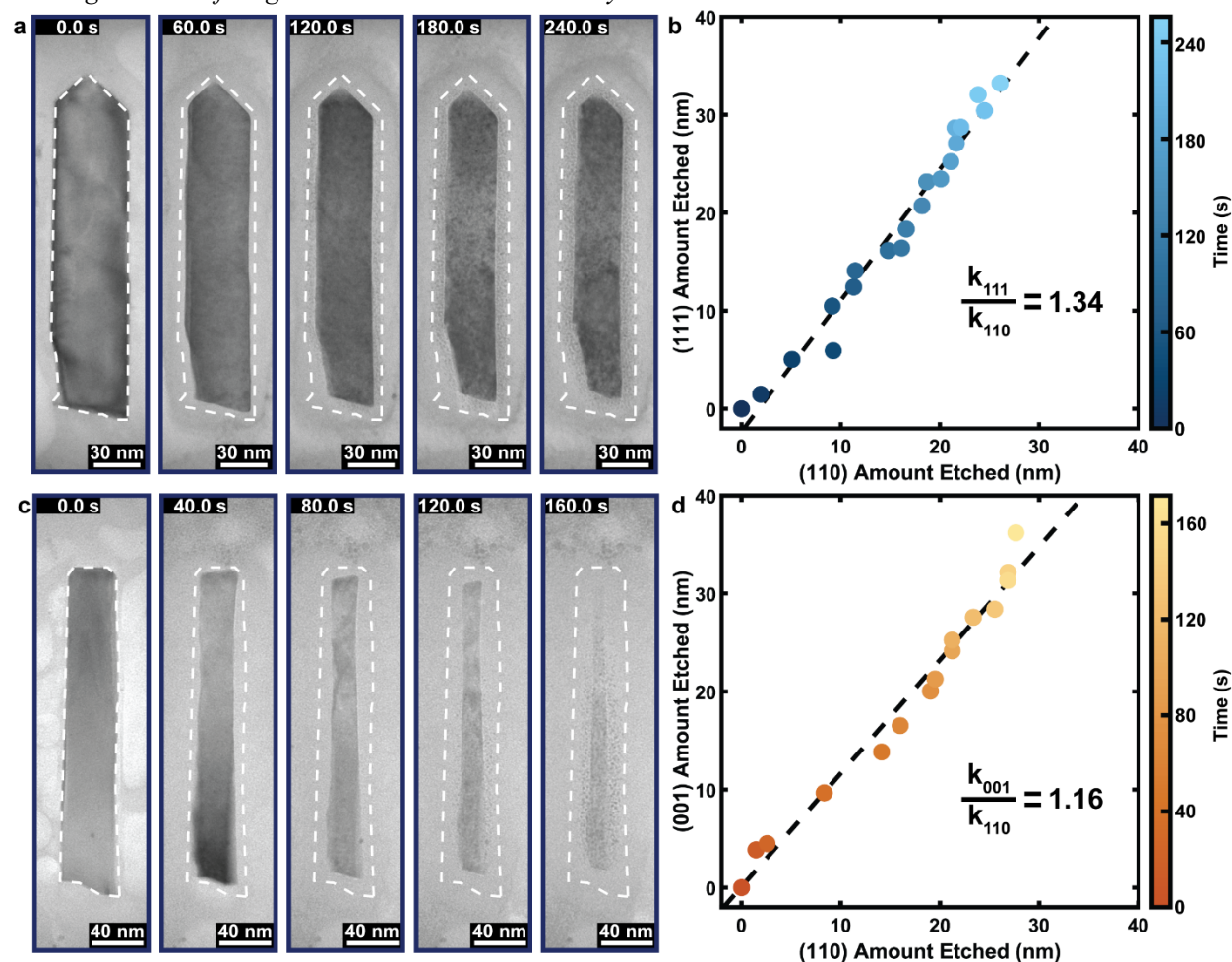
Fig. 3: Dissolution trajectories of individual nanocrystals in an Fe(III) electrolyte. (a) TEM image time series of a (111)-tipped nanocrystal. (b) Plot of the amount of (111) facet dissolved versus amount of (110) facet dissolved for the (111)-tipped nanocrystal. (c) TEM image time series of a (001)-tipped nanocrystal. (d) Amount of the (001) facet dissolved versus amount of (110) facet dissolved for the (001)-tipped nanocrystal.

Fig. 3a shows a TEM image time series collected for a (111)-tipped RuO_2 nanocrystal. The images indicate that the single-crystalline morphology was preserved with a well-defined projection observed throughout the dissolution trajectory. The images observed suggest an absence of substantial pitting, suggesting layer-by-layer dissolution of RuO_2 along low-index facets. We developed a methodology to quantify the change in nanocrystals dimensions over time (see Supplementary Information). The projection of the (111)-tipped RuO_2 nanocrystal could be described by the combination of two dimensions associated with (111) facets, and one dimension associated with (110) facets. Many nanocrystals displayed a slight delay in the onset of dissolution, as shown in Fig. S10 and Supplementary Movies S1-S2. The delay in dissolution could be associated with the time required to generate a steady-state concentration of oxidant, as has been previously observed via EELS for Ce redox additives.[28] After an initial delay there was a portion of the trajectory that exhibits substantial dissolution over time. This was followed by a gradual decrease in the dissolution rate over several minutes (Fig. S10). The decrease in dissolution rate was attributed to the formation of Ru dissolution products that physically excluded the Fe redox additive from the nanocrystal

surface, as evidenced by elemental mapping of the graphene liquid cell environment (Fig. 2b). We developed a kinetic model that incorporates the exclusion of Fe-based oxidants from the nanocrystal surface due to Ru dissolution product confinement near the nanocrystal surface (see Supplementary Information). The kinetic model was able to deconvolute the effect of oxidant exclusion, thus allowing the extraction of dissolution rates along facet pairs. The model exhibited agreement with the experimentally observed dissolution trajectories as shown on Fig. S10. To understand the selectivity of dissolution for different families of facets, we developed a method of analysis that was independent of the dissolution rate over time (see Supplementary Information). By plotting the amount of material dissolved along one crystallographic direction against the amount of material dissolved along another crystallographic direction for every time point, the selectivity between the facets was extracted for each nanocrystal from a linear fit of the dissolution data (Fig. 3b). Fig. 3c shows a TEM image time series collected for a (001)-tipped RuO_2 nanocrystal. Like the (111)-tipped nanocrystal shown in Fig. 3a, the images indicate the preservation of a well-defined projection at all time points. The projection of the (111)-tipped RuO_2 nanocrystals was described by the combination of one (001) dimension and one (110) dimension, representing the tips and sides of the nanocrystals, respectively. Many nanocrystals in the dataset had additional (111) facets that truncated the corners of nanocrystals—these facets were not analyzed in the focused (001) study. The delay in dissolution that was observed in the (111) dataset was also observed for the (001) dataset. Fig. 3d shows the dimension versus dimension plot for the nanocrystal shown in Fig. 3c, revealing the relative dissolution rate for this nanocrystal.
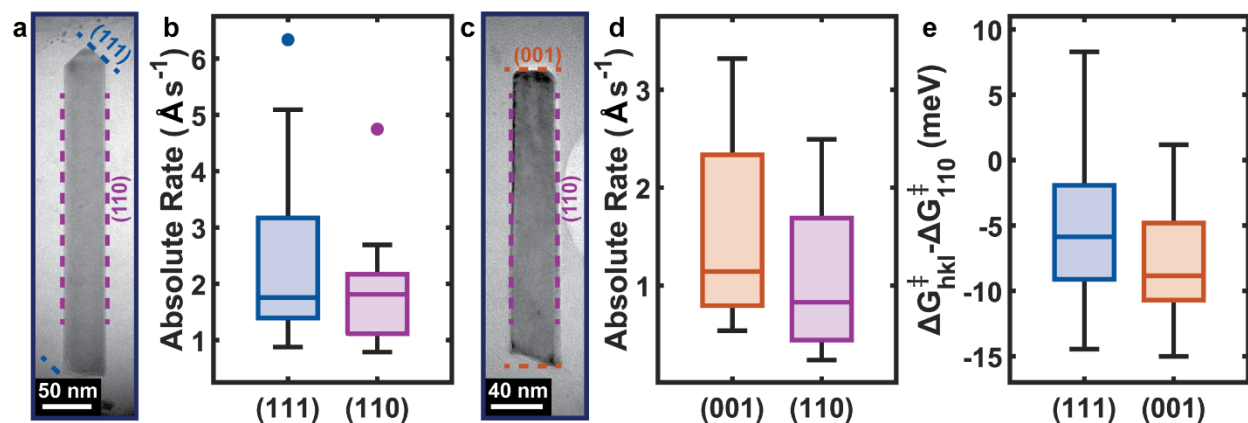

Fig. 4: Summary of the dissolution rates for the nanocrystals used in this study, classified by the facet defining the tip of the nanocrystal. (a) Representative nanocrystal showing the definitions of the (110) and (111) facets used in this study. (b) Dissolution rates observed for (111)-tipped RuO_2 nanocrystals along the (111) and (110) directions. (c) Representative nanocrystal showing the definitions of the (110) and (001) facets used in this study. (d) Dissolution rates observed for (001)-tipped RuO_2 nanocrystals along the (001) and (110) directions. (f) Relative facet stabilities, defined as the difference in energy for dissolution along the (hkl) facet as compared to along the (110) facet, observed for both (111)- and (001)-tipped RuO_2 nanocrystals.

Fig. 4 summarizes the absolute and relative facet stabilities observed for the RuO_2 nanocrystals studied herein. Nanocrystals were classified as either being tipped by (111) facets or by (001) facets. In some cases, crystals had a mixture of (111) facets and (001) facets. Since we found that more nanocrystals were (111)-tipped in our study, we included mixed-tipped nanocrystals in the (001)-tipped nanocrystal dataset to improve the statistics of the (001)-tipped dataset. The analysis included 13 nanocrystals in the (111)-tipped dataset, and 11 nanocrystals in the (001) dataset. Fig. S11 shows a summary of the sizes of the nanocrystals observed for the LP-TEM studies. The (111)-tipped nanocrystals exhibited widths of 24.5 ±

8.7 nm, lengths of 276.1 ± 54.2 nm, and aspect ratios of 13.5 ± 7.8, and the (001)-tipped nanocrystals exhibited widths of 29.3 ± 9.3 nm, lengths of 265.3 ± 96.3 nm, and aspect ratios of 9.5 ± 3.5. For (111)-tipped nanocrystals, we observed dissolution rates of 0.79 to 4.75 Å s^{-1} along the (110) facet, with a median value of 1.81 Å s^{-1}. We observed dissolution rates of 0.88 to 6.33 Å s^{-1} along the (111) facet, with a median value of 1.76 Å s^{-1} (Fig. 4b). While the absolute etching rates are influenced by various parameters such as the local concentration of oxidant, the relative dissolution rates are expected to be substantially less sensitive to the liquid cell environment and more sensitive to the intrinsic stability of the crystallographic facets. By tracking the dissolution trajectories of individual nanocrystals at each relevant crystallographic facet, we were able to determine the relative stability of each facet at the individual nanocrystal level (Fig. S12). In almost all cases, the (111) crystallographic facet was less stable than the (110) crystallographic facet. The relative dissolution rates range from 0.72 to 1.76 with a median relative rate of 1.26. Fig. 4d summarizes the statistical information of the individual nanocrystal trajectories for (001)-tipped nanocrystals. The dissolution rates along the (110) facet for the (001)-tipped nanocrystals ranged from 0.24 to 2.49 Å s^{-1}, with a median value of 0.83 Å s^{-1}. The absolute rate of dissolution along the (110) facet was over 100% faster for (111)-tipped nanocrystals and exhibited a wider distribution compared to (001)-tipped nanocrystals. The absolute dissolution rate along the (001) facet ranged from 0.54 to 3.32 Å s^{-1}, with a median value of 1.14 Å s^{-1}. The relative rate for (001) versus (110) ranged from 0.96 to 2.52, with a median value of 1.41 (Fig. S12). The results indicate that the *ensemble* of (110) facets exhibited the highest stability, followed by the (111) facets, and the (001) facets.

The relative dissolution rates exhibit a standard deviation that cannot be attributed to differences in oxidant concentrations between experiments, as these differences are accounted for by our analysis method as discussed in the Supplementary Information. These differences could arise from nanoscale heterogeneity present within a nanocrystal population, as has been previously observed for Pt nanocrystal systems.[41-43] We conducted geometric phase analysis (GPA) using the CrysTBox software to investigate the nanoscale structural heterogeneity present in our RuO$_2$ nanocrystal population (Fig. S13).[44] Simulated perfect nanocrystals displayed a narrow distribution of strain centered at ±0.00 in both the ε_{xx} and ε_{yy} directions (Fig. S14). The experimental nanocrystals showed a broader range of strain when compared to the perfect nanocrystals, and within the experimental dataset there was a wide range of relative strain (Fig. S13). While the strains were centered around 0.00, each nanocrystal exhibited a different strain standard deviation. The nanocrystals exhibited standard deviations from 0.07 to 0.11 along the ε_{xx} direction, and standard deviations from 0.07 to 0.10 along the ε_{yy} direction. The extremes in strain exhibited larger differences, with the 98th percentile of strain along the ε_{xx} and ε_{yy} directions ranging from 0.09 to 0.17, and the 2nd percentile ranging from -0.16 to -.09 (Fig. S13). Strain can alter the electronic structure of materials, which has been exploited to improve electrocatalyst activity.[45-47] Additional studies have indicated that strain can lead to strain-induced corrosion of electrochemical materials.[41] We developed a model based on fundamental thermodynamic and kinetic principles to understand the effects of strain on dissolution kinetics (see Supplementary Information). Our analysis indicates that both the average strain and the strain variance can contribute to accelerated dissolution. Studies have shown that increasing the annealing temperature of noble metal oxide films can increase stability, which would be consistent with a decrease in both the average strain and strain variance of an electrocatalyst material.[48]

The relative dissolution rates are an experimental observation of differences in the relative activation energy for dissolution between different sets of crystallographic facets in a single RuO$_2$ nanocrystal. The 0.72 to 1.76 relative dissolution rates observed for (111)-tipped nanocrystals correspond to an activation barrier energy difference for etching along the (111) dimension versus the (110) dimension of 8.3 to -14.5 meV, respectively. Overall, the (111) facets exhibit an *ensemble activation barrier* with a

median value of -5.9 meV lower than the activation barrier for (110) facet dissolution, with a standard deviation of 5.8 meV present due to nanoscale heterogeneity of the RuO_2 nanocrystals (Fig. 4e). The (001)-tipped nanocrystals exhibit relative dissolution rates for (001) facets versus (110) facets that range from 0.96 to 2.52, corresponding to activation barrier energy differences ranging from 1.2 meV to -23.8 meV, respectively. The (001) facets exhibit an ensemble activation barrier with a median value that is -8.8 meV lower than the activation barrier for the dissolution of (110) facets, with a standard deviation of 6.6 meV due to RuO_2 nanoscale heterogeneity (Fig. 4e). Overall, our study indicates that while the *ensemble stability* of RuO_2 nanocrystal facets increase from (001) < (111) < (110), there is a substantial overlap in the stability distributions which leads to inversions in the stability trends at the nanoscale.

Conclusions

The RuO_2 nanocrystals studied herein had a dispersion in stability across different low-index crystallographic facets, represented by the rate of dissolution along different directions. While the rutile (110) families of facets demonstrated higher ensemble stability than both the (111) and (001) families of facets, the stability relationship in individual nanocrystals was highly heterogeneous with some nanocrystals displaying an inverse stability relationship. Relative stabilities ranged from 8.3 to -14.5 meV and 1.2 to -23.8 meV for the (111) and (001) facets versus the (110) facet, respectively, leading to different relative rates of dissolution within individual nanocrystals. The direct observation of the dissolution of RuO_2 nanocrystals represents a key step in the ongoing challenge of understanding nanoscale heterogeneity and improving electrocatalyst activity and stability under operating conditions. The instrumental and analytical techniques developed in this study to analyze dissolution trajectories of anisotropic nanocrystals can be modified to interrogate other electrocatalysts or nanomaterials under operating conditions, enabling the direct integration of nanoscale observations in electrocatalyst discovery efforts.

Data availability statement

The LPTEM data that support the findings of this study are openly available in the Duke Research Data Repository.[49] This consists of the videos that were analyzed in the production of this study, stored as 1 frame s^{-1} and 1024x1024 px to meet institutional requirements for online storage. The full-fidelity dataset is available upon request. The MATLAB code used to analyze the LPTEM data and extract the kinetic parameters is openly available.[50]

Author Information

Department of Chemistry, Duke University, Durham, North Carolina 27708, United States

S. Avery Vigil, Ivan A. Moreno-Hernandez

Author Contributions

I. A. M.-H. conceived and supervised the research project. S. A. V. and I. A. M.-H. carried out the experiments, analyzed the data, and wrote and revised the manuscript.

Conflicts of interest

The authors declare no competing financial interest.

Acknowledgments

References

(1) Lewis, N. S. Research opportunities to advance solar energy utilization. *Science* **2016**, *351* (6271), aad1920.

(2) Chen, J. G.; Crooks, R. M.; Seefeldt, L. C.; Bren, K. L.; Bullock, R. M.; Darensbourg, M. Y.; Holland, P. L.; Hoffman, B.; Janik, M. J.; Jones, A. K.; et al. Beyond fossil fuel–driven nitrogen transformations. *Science* **2018**, *360* (6391), eaar6611.

(3) Zhao, G.; Huang, X.; Wang, X.; Wang, X. Progress in catalyst exploration for heterogeneous CO_2 reduction and utilization: a critical review. *J. Mater. Chem. A* **2017**, *5* (41), 21625-21649.

(4) Wu, J.; Huang, Y.; Ye, W.; Li, Y. CO_2 Reduction: From the Electrochemical to Photochemical Approach. *Adv. Sci.* **2017**, *4* (11), 1700194.

(5) Francke, R.; Schille, B.; Roemelt, M. Homogeneously Catalyzed Electroreduction of Carbon Dioxide—Methods, Mechanisms, and Catalysts. *Chem. Rev.* **2018**, *118* (9), 4631-4701.

(6) Qiao, J.; Liu, Y.; Hong, F.; Zhang, J. A review of catalysts for the electroreduction of carbon dioxide to produce low-carbon fuels. *Chem. Soc. Rev.* **2014**, *43* (2), 631-675.

(7) Ouimet, R. J.; Glenn, J. R.; De Porcellinis, D.; Motz, A. R.; Carmo, M.; Ayers, K. E. The Role of Electrocatalysts in the Development of Gigawatt-Scale PEM Electrolyzers. *ACS Catal.* **2022**, 6159-6171.

(8) Chatenet, M.; Pollet, B. G.; Dekel, D. R.; Dionigi, F.; Deseure, J.; Millet, P.; Braatz, R. D.; Bazant, M. Z.; Eikerling, M.; Staffell, I.; et al. Water electrolysis: from textbook knowledge to the latest scientific strategies and industrial developments. *Chem. Soc. Rev.* **2022**, *51* (11), 4583-4762.

(9) Zhao, Y.; Adiyeri Saseendran, D. P.; Huang, C.; Triana, C. A.; Marks, W. R.; Chen, H.; Zhao, H.; Patzke, G. R. Oxygen Evolution/Reduction Reaction Catalysts: From *In Situ* Monitoring and Reaction Mechanisms to Rational Design. *Chem. Rev.* **2023**, *123* (9), 6257-6358.

(10) Gunasooriya, G. T. K. K.; Nørskov, J. K. Analysis of Acid-Stable and Active Oxides for the Oxygen Evolution Reaction. *ACS Energy Lett.* **2020**, *5* (12), 3778-3787.

(11) Song, J.; Wei, C.; Huang, Z.-F.; Liu, C.; Zeng, L.; Wang, X.; Xu, Z. J. A review on fundamentals for designing oxygen evolution electrocatalysts. *Chem. Soc. Rev.* **2020**, *49* (7), 2196-2214.

(12) Audichon, T.; Napporn, T. W.; Canaff, C.; Morais, C.; Comminges, C.; Kokoh, K. B. IrO_2 Coated on RuO_2 as Efficient and Stable Electroactive Nanocatalysts for Electrochemical Water Splitting. *J. Phys. Chem. C* **2016**, *120* (5), 2562-2573.

(13) Suen, N.-T.; Hung, S.-F.; Quan, Q.; Zhang, N.; Xu, Y.-J.; Chen, H. M. Electrocatalysis for the oxygen evolution reaction: recent development and future perspectives. *Chem. Soc. Rev.* **2017**, *46* (2), 337-365.

(14) Wang, M.; Wa, Q.; Bai, X.; He, Z.; Samarakoon, W. S.; Ma, Q.; Du, Y.; Chen, Y.; Zhou, H.; Liu, Y.; et al. The Restructuring-Induced CoO_x Catalyst for Electrochemical Water Splitting. *JACS Au* **2021**, *1* (12), 2216-2223.

(15) Ding, H.; Liu, H.; Chu, W.; Wu, C.; Xie, Y. Structural Transformation of Heterogeneous Materials for Electrocatalytic Oxygen Evolution Reaction. *Chem. Rev.* **2021**, *121* (21), 13174-13212.

(16) Klyukin, K.; Zagalskaya, A.; Alexandrov, V. Role of Dissolution Intermediates in Promoting Oxygen Evolution Reaction at $RuO_2(110)$ Surface. *J. Phys. Chem. C* **2019**, *123* (36), 22151-22157.

(17) Rao, R. R.; Kolb, M. J.; Halck, N. B.; Pedersen, A. F.; Mehta, A.; You, H.; Stoerzinger, K. A.; Feng, Z.; Hansen, H. A.; Zhou, H.; et al. Towards identifying the active sites on $RuO_2(110)$ in catalyzing oxygen evolution. *Energy Environ. Sci.* **2017**, *10* (12), 2626-2637.

(18) Zhu, Y.; Kuo, T.-R.; Li, Y.-H.; Qi, M.-Y.; Chen, G.; Wang, J.; Xu, Y.-J.; Chen, H. M. Emerging dynamic structure of electrocatalysts unveiled by *in situ* X-ray diffraction/absorption spectroscopy. *Energy Environ. Sci.* **2021**, *14* (4), 1928-1958.

(19) Rao, R. R.; Kolb, M. J.; Giordano, L.; Pedersen, A. F.; Katayama, Y.; Hwang, J.; Mehta, A.; You, H.; Lunger, J. R.; Zhou, H.; et al. Operando identification of site-dependent water oxidation activity on ruthenium dioxide single-crystal surfaces. *Nat. Catal.* **2020**, *3* (6), 516-525.

(20) Bard, A. J.; Parsons, R.; Jordan, J. *Standard Potentials in Aqueous Solution*; Marcel Dekker, 1985.

(21) Lee, Y.; Suntivich, J.; May, K. J.; Perry, E. E.; Shao-Horn, Y. Synthesis and Activities of Rutile IrO_2 and RuO_2 Nanoparticles for Oxygen Evolution in Acid and Alkaline Solutions. *J. Phys. Chem. Lett.* **2012**, *3* (3), 399-404.

(22) Roy, C.; Rao, R. R.; Stoerzinger, K. A.; Hwang, J.; Rossmeisl, J.; Chorkendorff, I.; Shao-Horn, Y.; Stephens, I. E. L. Trends in Activity and Dissolution on RuO_2 under Oxygen Evolution Conditions: Particles versus Well-Defined Extended Surfaces. *ACS Energy Lett.* **2018**, *3* (9), 2045-2051.

(23) Rao, R. R.; Kolb, M. J.; Hwang, J.; Pedersen, A. F.; Mehta, A.; You, H.; Stoerzinger, K. A.; Feng, Z.; Zhou, H.; Bluhm, H.; et al. Surface Orientation Dependent Water Dissociation on Rutile Ruthenium Dioxide. *J. Phys. Chem. C* **2018**, *122* (31), 17802-17811.

(24) Stoerzinger, K. A.; Diaz-Morales, O.; Kolb, M.; Rao, R. R.; Frydendal, R.; Qiao, L.; Wang, X. R.; Halck, N. B.; Rossmeisl, J.; Hansen, H. A.; et al. Orientation-Dependent Oxygen Evolution on RuO_2 without Lattice Exchange. *ACS Energy Lett.* **2017**, *2* (4), 876-881.

(25) Stoerzinger, K. A.; Qiao, L.; Biegalski, M. D.; Shao-Horn, Y. Orientation-Dependent Oxygen Evolution Activities of Rutile IrO_2 and RuO_2. *J. Phys. Chem. Lett.* **2014**, *5* (10), 1636-1641.

(26) Jin, R.; Higaki, T. Open questions on the transition between nanoscale and bulk properties of metals. *Commun. Chem.* **2021**, *4* (1), 28.

(27) Moreno-Hernandez, I. A.; Crook, M. F.; Jamali, V.; Alivisatos, A. P. Recent advances in the study of colloidal nanocrystals enabled by *in situ* liquid-phase transmission electron microscopy. *MRS Bull.* **2022**, *47* (3), 305-313.

(28) Crook, M. F.; Moreno-Hernandez, I. A.; Ondry, J. C.; Ciston, J.; Bustillo, K. C.; Vargas, A.; Alivisatos, A. P. EELS Studies of Cerium Electrolyte Reveal Substantial Solute Concentration Effects in Graphene Liquid Cells. *J. Am. Chem. Soc.* **2023**, *145* (12), 6648-6657.

(29) Moreno-Hernandez, I. A.; Crook, M. F.; Ondry, J. C.; Alivisatos, A. P. Redox Mediated Control of Electrochemical Potential in Liquid Cell Electron Microscopy. *J. Am. Chem. Soc.* **2021**, *143* (31), 12082-12089.

(30) Lee, Y.; Ye, B.-U.; Yu, H. K.; Lee, J.-L.; Kim, M. H.; Baik, J. M. Facile Synthesis of Single Crystalline Metallic RuO_2 Nanowires and Electromigration-Induced Transport Properties. *J. Phys. Chem. C* **2011**, *115* (11), 4611-4615.

(31) Hauwiller, M. R.; Ondry, J. C.; Alivisatos, A. P. Using Graphene Liquid Cell Transmission Electron Microscopy to Study *in Situ* Nanocrystal Etching. *J. Vis. Exp.* **2018**, (135).

(32) Hauwiller, M. R.; Ondry, J. C.; Chan, C. M.; Khandekar, P.; Yu, J.; Alivisatos, A. P. Gold Nanocrystal Etching as a Means of Probing the Dynamic Chemical Environment in Graphene Liquid Cell Electron Microscopy. *J. Am. Chem. Soc.* **2019**, *141* (10), 4428-4437.

(33) Morgan, D. J. Resolving ruthenium: XPS studies of common ruthenium materials. *Surf. Interface Anal.* **2015**, *47* (11), 1072-1079.

(34) Ferrari, A. C.; Meyer, J. C.; Scardaci, V.; Casiraghi, C.; Lazzeri, M.; Mauri, F.; Piscanec, S.; Jiang, D.; Novoselov, K. S.; Roth, S.; et al. Raman spectrum of graphene and graphene layers. *Phys. Rev. Lett.* **2006**, *97* (18), 187401.

(35) Chen, R. S.; Chen, C. C.; Huang, Y. S.; Chia, C. T.; Chen, H. P.; Tsai, D. S.; Tiong, K. K. A comparative study of microstructure of RuO_2 nanorods via Raman scattering and field emission scanning electron microscopy. *Solid State Commun.* **2004**, *131* (6), 349-353.

(36) Crook, M. F.; Laube, C.; Moreno-Hernandez, I. A.; Kahnt, A.; Zahn, S.; Ondry, J. C.; Liu, A.; Alivisatos, A. P. Elucidating the Role of Halides and Iron during Radiolysis-Driven Oxidative Etching of Gold Nanocrystals Using Liquid Cell Transmission Electron Microscopy and Pulse Radiolysis. *J. Am. Chem. Soc.* **2021**, *143* (30), 11703-11713.

(37) Hauwiller, M. R.; Frechette, L. B.; Jones, M. R.; Ondry, J. C.; Rotskoff, G. M.; Geissler, P.; Alivisatos, A. P. Unraveling Kinetically-Driven Mechanisms of Gold Nanocrystal Shape Transformations Using Graphene Liquid Cell Electron Microscopy. *Nano Lett.* **2018**, *18* (9), 5731-5737.

(38) Ye, X.; Jones, M. R.; Frechette, L. B.; Chen, Q.; Powers, A. S.; Ercius, P.; Dunn, G.; Rotskoff, G. M.; Nguyen, S. C.; Adiga, V. P.; et al. Single-particle mapping of nonequilibrium nanocrystal transformations. *Science* **2016**, *354* (6314), 874-877.

(39) Schneider, N. M.; Norton, M. M.; Mendel, B. J.; Grogan, J. M.; Ross, F. M.; Bau, H. H. Electron–Water Interactions and Implications for Liquid Cell Electron Microscopy. *J. Phys. Chem. C* **2014**, *118* (38), 22373-22382.

(40) Malis, T.; Cheng, S. C.; Egerton, R. F. EELS log-ratio technique for specimen-thickness measurement in the TEM. *J. Electron. Microsc. Tech.* **1988**, *8* (2), 193-200.

(41) Shi, F.; Gao, W.; Shan, H.; Li, F.; Xiong, Y.; Peng, J.; Xiang, Q.; Chen, W.; Tao, P.; Song, C.; et al. Strain-Induced Corrosion Kinetics at Nanoscale Are Revealed in Liquid: Enabling Control of Corrosion Dynamics of Electrocatalysis. *Chem.* **2020**, *6* (9), 2257-2271.

(42) Park, J.; Elmlund, H.; Ercius, P.; Yuk, J. M.; Limmer, D. T.; Chen, Q.; Kim, K.; Han, S. H.; Weitz, D. A.; Zettl, A.; et al. 3D structure of individual nanocrystals in solution by electron microscopy. *Science* **2015**, *349* (6245), 290-295.

(43) Kim, B. H.; Heo, J.; Kim, S.; Reboul, C. F.; Chun, H.; Kang, D.; Bae, H.; Hyun, H.; Lim, J.; Lee, H.; et al. Critical differences in 3D atomic structure of individual ligand-protected nanocrystals in solution. *Science* **2020**, *358* (6486), 60-67.

(44) Klinger, M. More features, more tools, moreCrysTBox. *J. Appl. Crystallogr.* **2017**, *50* (4), 1226-1234.

(45) You, B.; Tang, M. T.; Tsai, C.; Abild-Pedersen, F.; Zheng, X.; Li, H. Enhancing Electrocatalytic Water Splitting by Strain Engineering. *Adv. Mater.* **2019**, *31* (17), e1807001.

(46) Maiti, S.; Maiti, K.; Curnan, M. T.; Kim, K.; Noh, K.-J.; Han, J. W. Engineering electrocatalyst nanosurfaces to enrich the activity by inducing lattice strain. *Energy Environ. Sci.* **2021**, *14* (7), 3717-3756, 10.1039/D1EE00074H.

(47) Liu, X.; Zhang, L.; Zheng, Y.; Guo, Z.; Zhu, Y.; Chen, H.; Li, F.; Liu, P.; Yu, B.; Wang, X.; et al. Uncovering the Effect of Lattice Strain and Oxygen Deficiency on Electrocatalytic Activity of Perovskite Cobaltite Thin Films. *Adv. Sci.* **2019**, *6* (6), 1801898.

(48) Geiger, S.; Kasian, O.; Shrestha, B. R.; Mingers, A. M.; Mayrhofer, K. J. J.; Cherevko, S. Activity and Stability of Electrochemically and Thermally Treated Iridium for the Oxygen Evolution Reaction. *J. Electrochem. Soc.* **2016**, *163* (11), F3132-F3138.

(49) Vigil, S. A.; Moreno-Hernandez, I. A. Data from: "Dissolution heterogeneity observed in anisotropic ruthenium dioxide nanocrystals via liquid-phase transmission electron microscopy". *Duke Research Data Repository*. Duke University, **2023.** https://doi.org/10.7924/r47h1sc26.

(50) Vigil, S. A.; Moreno-Hernandez, I. A. *RuO2_Dissolution*. Github Repository, **2023**. https://github.com/morenohernandezlab/RuO2_Dissolution.